

Article

Characterization of Macro Mechanical Properties and Microstructures of Cement-Based Composites Prepared from Fly Ash, Gypsum and Steel Slag

Jiajian Li ^{1,2}, Shuai Cao ^{1,2,*} and Erol Yilmaz ^{3,*}

¹ School of Civil and Resources Engineering, University of Science and Technology Beijing, Beijing 100083, China; lijiajian0123@163.com

² State Key Laboratory of High-Efficient Mining and Safety of Metal Mines, Ministry of Education, University of Science and Technology Beijing, Beijing 100083, China

³ Department of Civil Engineering, Geotechnical Division, Recep Tayyip Erdogan University, Fener, Rize TR53100, Turkey

* Correspondence: sandy_cao@ustb.edu.cn (S.C.); erol.yilmaz@erdogan.edu.tr (E.Y.)

Abstract: Using solid wastes (SWs) as backfilling material to fill underground mined-out areas (UMOAs) solved the environmental problems caused by SWs and reduced the backfilling cost. In this study, fly ash (FA), gypsum and steel slag (SS) were used to prepare cement-based composites (CBC). The uniaxial compression, computed tomography (CT) and scanning electron microscope (SEM) laboratory experiments were conducted to explore the macro and micromechanical properties of CBC. The findings showed that the uniaxial compressive strength (UCS) of CBC with a curing time of 7 d could reach 6.54 MPa. The increase of SS content reduced the UCS of CBC, while the gypsum and FA content could increase the UCS of CBC. Microscopic studies have shown that the SS particles in CBC have noticeable sedimentation, and the increase of SS content causes the failure mode of CBC from tensile to tensile-shear. These research results can provide a scientific reference for the preparation of backfilling materials.

Keywords: cement-based composites (CBC); industrial computed tomography; microstructural analysis; failure modes



Citation: Li, J.; Cao, S.; Yilmaz, E. Characterization of Macro Mechanical Properties and Microstructures of Cement-Based Composites Prepared from Fly Ash, Gypsum and Steel Slag. *Minerals* **2022**, *12*, 6. <https://doi.org/10.3390/min12010006>

Academic Editor: Abbas Taheri

Received: 22 November 2021

Accepted: 17 December 2021

Published: 21 December 2021

Publisher's Note: MDPI stays neutral with regard to jurisdictional claims in published maps and institutional affiliations.



Copyright: © 2021 by the authors. Licensee MDPI, Basel, Switzerland. This article is an open access article distributed under the terms and conditions of the Creative Commons Attribution (CC BY) license (<https://creativecommons.org/licenses/by/4.0/>).

1. Introduction

The development of mineral resources has brought great convenience to human life and caused severe environmental problems, such as groundwater pollution, air pollution, occupying farmland and solid waste (SWs) storage [1–3]. Among them, the environmental pollution caused by solid waste (SW) storage is severe. Moreover, solid waste includes many types, including tailings and waste rock from mines, fly ash (FA) from power plants, gypsum, steel slag (SS) or water quenched slag from smelters [4–9]. Statistically, the estimated accumulation of FA in China will reach more than 3 billion tons in 2020 [10]. However, the harmful elements in FA will have a severe impact on the surrounding water resources and soil environment after being washed by rain. In addition, dust will also cause severe pollution to the atmosphere.

In recent years, the concept of a waste-free city (WFC) has put forward higher requirements for solid waste resource utilization. Baotou is one of the pilot WFCs in Inner Mongolia, China. Moreover, FA and gypsum are the two main types of solid waste in Baotou [11]. Thus, the utilization of SWs has become a hot research topic in this city. The cyanide-containing tailings from gold mines cannot be used as backfill materials for underground mined-out areas for metal mines. This also led to the change in the mining method for these mines. Can we consider using SWs to prepare backfilling materials, thereby reducing safety risks and increasing ore recovery rates? This is the main topic for this paper.

Many scholars have researched FA and gypsum, including the chemical composition, cement substitute and direction preparation, mechanical characteristics and microstructural properties [12–17]. It is expected that the promotion and application of FA and gypsum to create the practical cementitious binder would become feasible [18]. Li et al. [19] believed that it is possible to prepare eco-friendly road base materials with FA and gypsum. Moreover, Wang et al. [20] developed a green binder system based on FA and gypsum incorporating slag or SS powders. Wansom et al. [21] found that the paste with gypsum: FA: ordinary Portland cement = 20:40:40 at the water/binder ratio of 0.5 showed the highest compressive strength and the most improved water resistance.

This study aimed to explore the feasibility of preparing cemented composites with FA, gypsum and SS. In this study, four kinds of cement-to-SW ratios were considered. The uniaxial compressive test, computed tomography (CT) scanning and scanning electron microscope (SEM) test were used to investigate the uniaxial compressive strength (UCS) and elastic modulus, distribution of SS particle, failure modes and hydrate products. This finding in this study can supply a reliable reference to backfilling material preparation for underground mined-out areas.

2. Materials and Methods

2.1. Materials

Three solid wastes, including FA, gypsum and SS, were used to prepare cement-based backfilling materials. The ordinary Portland cement named 42.5 R was used as cementitious material and tap water was used as mixing water in this study. The particle size distributions of FA, gypsum and SS were measured by the LS-POP (9) laser particle size analyzer (OMEC, Zhuhai, China). The particle size distributions of the above three types of solid wastes were shown in Figure 1 and Table 1.

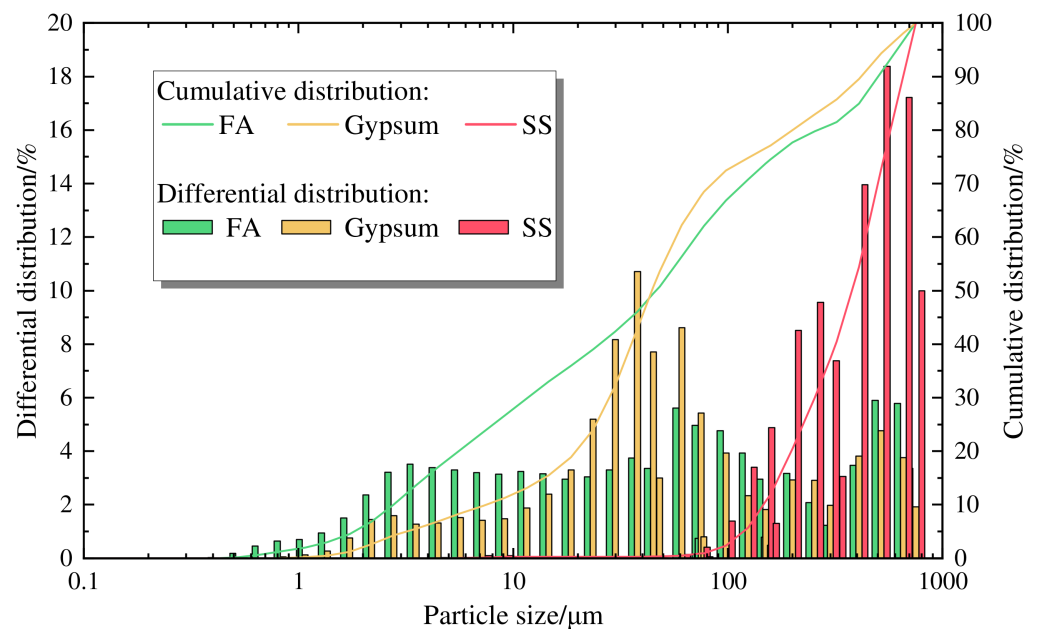


Figure 1. The solid waste particle size distribution.

Table 1. Physical parameters of the tested solid waste.

Solid Waste	D ₁₀ (μm)	D ₃₀ (μm)	D ₅₀ (μm)	D ₆₀ (μm)	D ₉₀ (μm)
FA	2.766	11.584	46.466	71.353	501.330
Gypsum	7.422	27.763	44.112	56.837	417.245
SS	149.923	253.382	357.429	435.956	656.526

In this study, the sequential X-ray fluorescence spectrometer from the University of Science and Technology Beijing (USTB) was used to investigate the chemical composition. The sequential X-ray fluorescence spectrometer adopts fully automatic computer control. The leading technical indicators include a maximum power of 60 kV, a scan speed of 300°/min and a current of 140 mA. Figure 2 shows the XRD (X-ray diffraction) result of SS. The principal oxides are shown in Table 2.

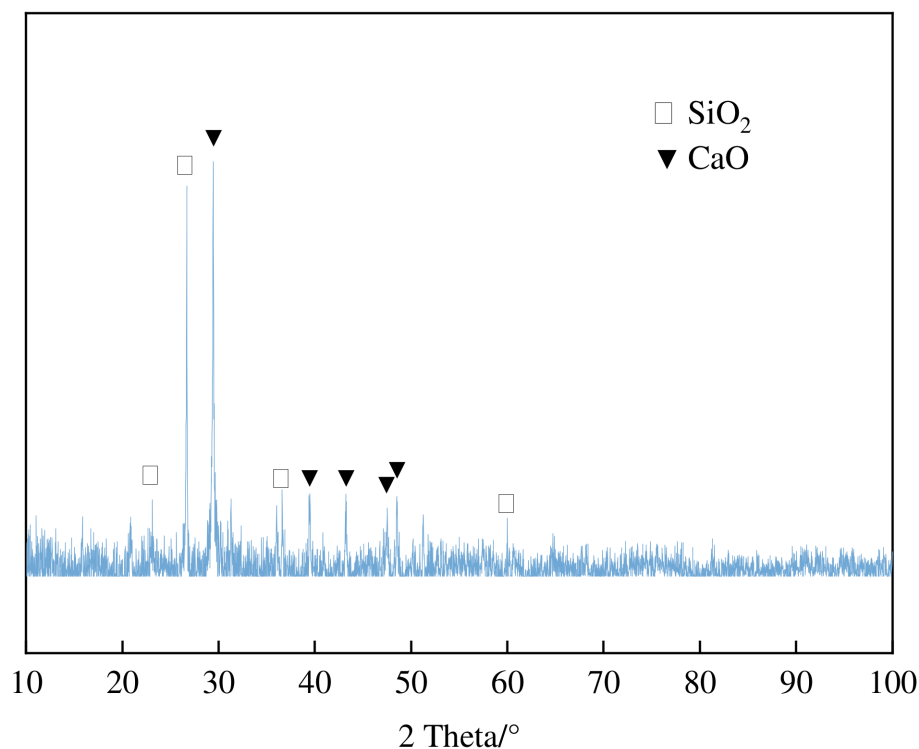


Figure 2. The XRD spectra image of the tested SS.

Table 2. Main oxide of the gypsum, FA, SS and cement (unit: wt. %).

Materials	SiO ₂	Al ₂ O ₃	CaO	Fe ₂ O ₃	MgO	K ₂ O	SO ₃	TiO ₂	Na ₂ O
Cement	19.69	5.63	58.22	2.89	4.63	0.97	2.50	0.90	1.19
FA	51.50	19.43	13.85	7.54	2.81	1.27	1.18	0.91	0.90
Gypsum	6.66	2.58	44.12	1.15	1.86	0.86	41.20	0.17	0.27
SS	36.10	9.77	40.30	0.60	7.27	0.63	1.59	1.24	0.60

2.2. Specimen Preparation and Curing Conditions

The raw materials used in the present study were gypsum, FA, SS, cement and water. The CBC samples were divided into four groups based on the different cement-to-solid waste (C/SW) ratio (A–D). The C/SW ratio and the ratio of gypsum, FA and SS are shown in Table 3. The CBC samples were prepared in this study according to GB/50152-92 [22,23]. The solid content of the CBC was 70 wt. % and the curing time was 7 d. The diameter and height of the selected molds were 50 mm and 100 mm [24]. Then, we mixed the raw materials for 5 min and poured them into the molds. To facilitate the removal of the molds, the lubricant was evenly spread on the inner wall of the molds in advance. Moreover, the tested CBC specimens were placed in a curing box with a temperature of 20 ± 2 °C and a humidity of 98% during the whole curing process. Finally, the CBC specimens were demolded after 48 h. The CBC specimen preparation process is shown in Figure 3. It was found that the non-cement-based composite (NCBC) was not solidified after 48 h during the sample preparation process. Thus, we demolded the NCBC specimens when the curing time reached 7 days.

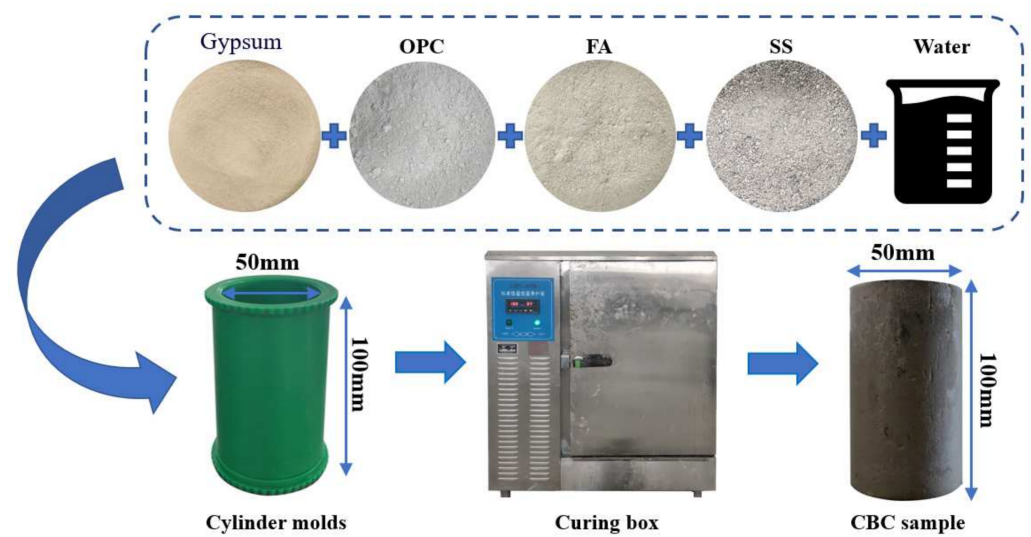


Figure 3. Flow chart of CBC specimen preparation.

Table 3. Mixture proportions of the CBC samples used in the experiments.

No.	C/SW Ratio	Type of Solid Waste			Water (wt. %)
		Gypsum (wt. %)	FA (wt. %)	SS (wt. %)	
A ₁	1:04	10	40	50	30
A ₂		10	50	40	
A ₃		20	40	40	
B ₁	1:08	10	40	50	
B ₂		10	50	40	
B ₃		20	40	40	
C ₁	1:12	10	40	50	
C ₂		10	50	40	
C ₃		20	40	40	
D ₁	No cement	10	40	50	
D ₂		10	50	40	
D ₃		20	40	40	

2.3. Uniaxial Compressive Strength Test

The uniaxial compression strength (UCS) experiment was performed using a universal digitally controlled uniaxial compressive test system with a range of 200 kN, according to GB/T 17671-1999 [25]. To obtain accurate experimental data, both ends of the CBC specimens were polished. Then, the loading rate was 1 mm/min during the whole experiment process. The UCS and stress–strain curves of the CBC specimen were obtained by the computer acquisition system. The slope of the linear elastic stage of the stress–strain curve was the elastic modulus of the CBC specimen.

2.4. X-ray CT Scanning Test

To explore the sizes and locations of internal cracks and pores, the industrial computed tomography (CT) system named IPT 61 series (GRANPECT company limited, Beijing, China) was used to detect the failure of the CBC sample after the UCS test [26]. The industrial computer tomography system could accurately and intuitively display the internal structure of the detected object in the form of a two-dimensional tomographic image or a three-dimensional image under the condition of no damage to the detected object. Moreover, the basic physical parameters were as follows: the light source, X-ray energy, spatial resolution, ambient temperature and density resolution were 450 kV, 2.5 LP/mm, 25 °C and 0.5%, respectively. Finally, the related scanning data and images could be recorded and saved into the computer.

2.5. Scanning Electron Microscope (SEM) Test

In this section, the cube CBC samples were selected to investigate the microstructures. Diamond was sprayed on the tested samples' surface to enhance its conductivity. A Scanning Electron Microscope (SEM) named ZEISS EVO18 in the Material Testing Center of USTB was conducted. The physical parameters were shown as follows: the acceleration voltage, magnification and resolution were 20 kV, 2000 times and 3 nm, respectively.

3. Results and Discussion

3.1. Effect of Cement, Gypsum, Fly Ash and Steel Slag on Uniaxial Compressive Strength

Figure 4 shows the UCS test results of CBC samples with different C/SW ratios. It could be found that the UCS increased when cement content increased. The UCS values of varied CBC samples were between 1.16 and 2.21 MPa when the C/SW ratio was 1:12. Besides, the UCS values of various CBC samples were between 4.83 and 6.54 MPa when the C/SW ratio was 1:04. In addition, the corresponding UCS values increased by two to three times when the C/SW ratio increased from 1:12 to 1:04.

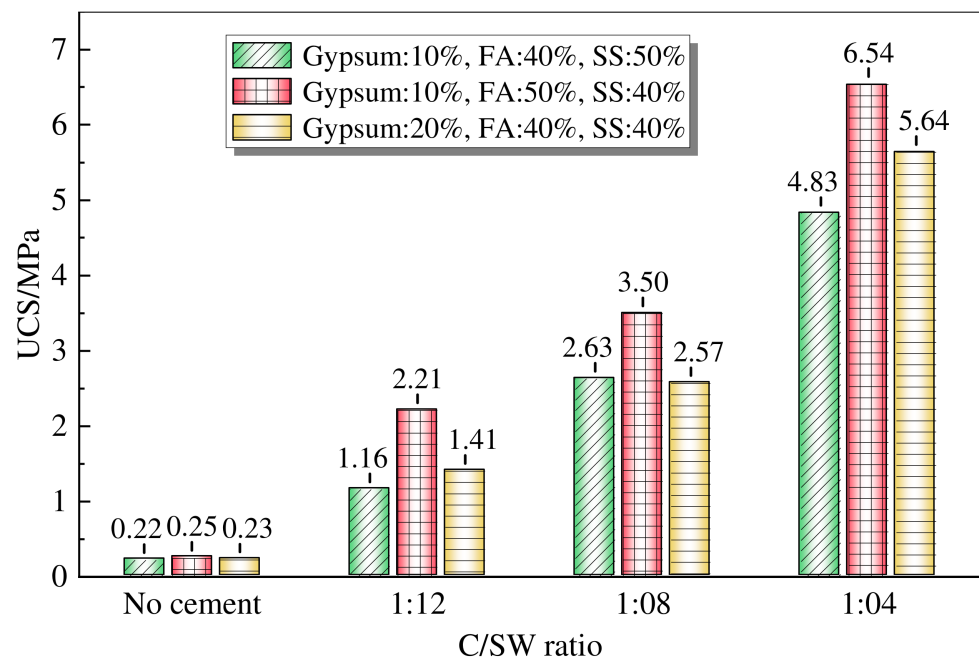


Figure 4. The linear fitting result between the UCS and C/SW ratio value.

In addition, it can also be found that both reducing gypsum or SS and increasing FA could lead to an increase in UCS values. However, reducing SS content and increasing gypsum could also improve the UCS values of tested specimens when the FA was a constant value.

The main reason was that the main components of FA were CaO, Al₂O₃ and SiO₂, which were similar to the chemical composition of cement. Thus, the FA could be added as a cementitious material instead of cement according to the related references [27,28]. Besides, the FA particles were fine particles and the unreacted FA particles could fill the pores between gypsum and SS particles. However, the chemical composition of gypsum was mainly CaSO₄, which did not participate in the hydration reaction in CBC specimens.

3.2. Effect of Cement, Gypsum, Fly Ash and Steel Slag on the Elastic Modulus

The elastic modulus values of CBC specimens were calculated according to the slope of stress–strain curves during the linear elastic stage. Figure 5 showed the relation between the elastic modulus and the C/SW ratio.

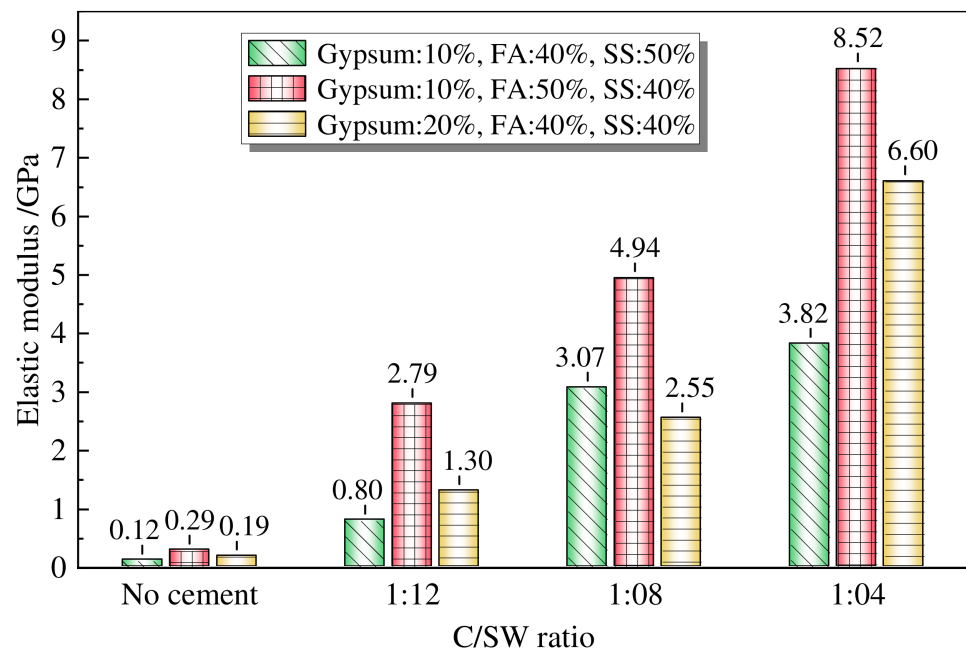


Figure 5. The power fitting relationship between the elastic modulus and C/SW ratio.

As shown in Figure 5, it was also found that the elastic modulus improvement law of CBC specimens varied with the C/SW ratios, similar to the UCS. That is, the elastic modulus values increased when the C/SW ratios increased accordingly. Besides, the elastic modulus of CBC was 0.80 to 2.79 GPa and 3.82 to 8.52 GPa when the C/SW ratios were 1:12 and 1:04, respectively. Besides, the corresponding elastic modulus values increased by two to four times when the C/SW ratio increased from 1:12 to 1:04. Increasing the contents of cement, FA and gypsum could effectively increase the elastic modulus of a CBC. The findings showed that the mechanical properties of CBC can be noticeably improved. This can also be very beneficial for controlling surface subsidence and rock movement caused by mining activities [29].

3.3. Industrial Computed Tomography Scanning Analysis of Cement-Based Composite Samples

Considering many specimens were scanned this time, the CT test system was used to investigate the spatial distribution of SS particles and crack locations in CBC when the C/SW ratio was 1:12. The X-rays scanned the specimen from bottom to top during the scanning process. The specimens were sliced and saved at an axial distance of 1 mm after scanning. Besides, the Image J software was used to distinguish the particle size and crack location on the cross-section. A pseudo color enhancing algorithm was used to process the original images.

3.3.1. Effect of Steel Slag Particle Content on Its Spatial Distribution

Figure 6 shows the slice data of various CBC specimens when the axial direction height was 90 mm, 75 mm, 50 mm, 25 mm and 10 mm.

It was found that the CT test results were much better at distinguishing due to the large size of the SS particles. Here, the yellow parts in the images were the SS particles and the blue parts represented the other substances and cracks in the CBC. It could also be obtained that the distribution of SS particles was different in various heights. The percentage of SS particles increased significantly when the height decreased because the SS particles settled during the CBC solidification process. The sedimentation law of SS particles was quantitatively characterized by the percentage of the area of SS particles in the slices.

Figure 7 shows the relationship between the SS percentage and the height of the CBC specimens.

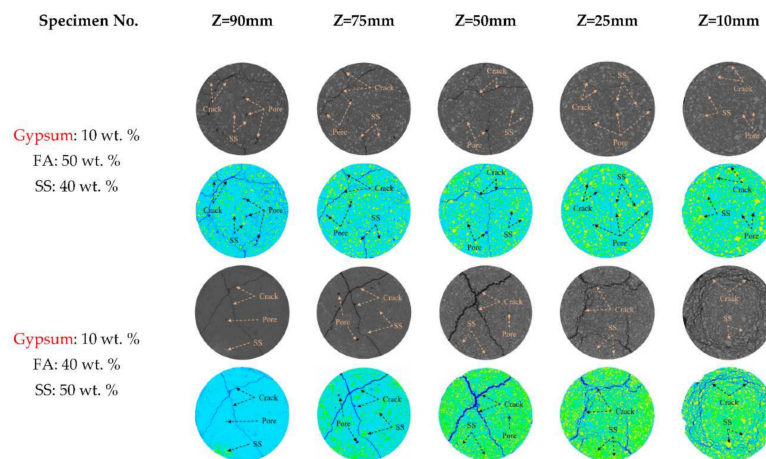


Figure 6. The CT images of different heights of CBC samples (C/SW ratio was 1:12).

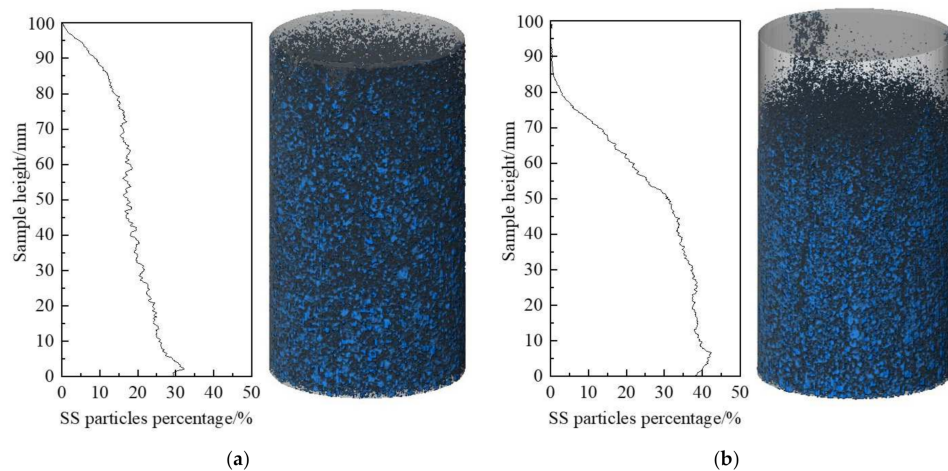


Figure 7. Distribution law of SS particles at different heights. (a) Gypsum: 10 wt. %, FA: 50 wt. % and SS: 40 wt. %; (b) Gypsum: 10 wt. %, FA: 40 wt. % and SS: 50 wt. %.

It could be seen that the percentage of SS particles of the CBC was the lowest at the top section, and the area of the SS particles was less than 5% of the cross-sectional area. The percentage of the SS particles of the CBC was the highest at the bottom section, accounting for about 30% to 40% of the cross-sectional area. The percentage of SS particles at different heights increased linearly as the height decreased when the SS content in CBC was 40 wt. %. For every 10 mm reduction in height, the percentage of SS particles increased by about 3%. The percentage of SS particles at different heights increased non-linearly when the height decreased when the SS content in CBC was 50 wt. %. The percentage of SS particles was above 30% when the height was between 0 and 50 mm, which indicated that the increase in the content of SS particles in CBC led to more obvious sedimentation of SS particles during the curing process.

The settlement of SS particles weakened the mechanical strength of the cement-based backfilling materials. However, the sedimentation of the coarse SS particles can cause difficulties, including pipeline blockage in pipeline slurry transportation [30]. Thus, the ratio of raw backfilling materials should be further optimized to reduce the sedimentation of SS particles in the future.

3.3.2. Effect of Steel Slag on Failure Modes of Cement-Based Composite Samples

Figure 8 shows the physical view (a and d), perspective view (b and e) and fracture view (c and f) of CBC specimens when the SS content was 40 wt. % and 50 wt. %, respectively.

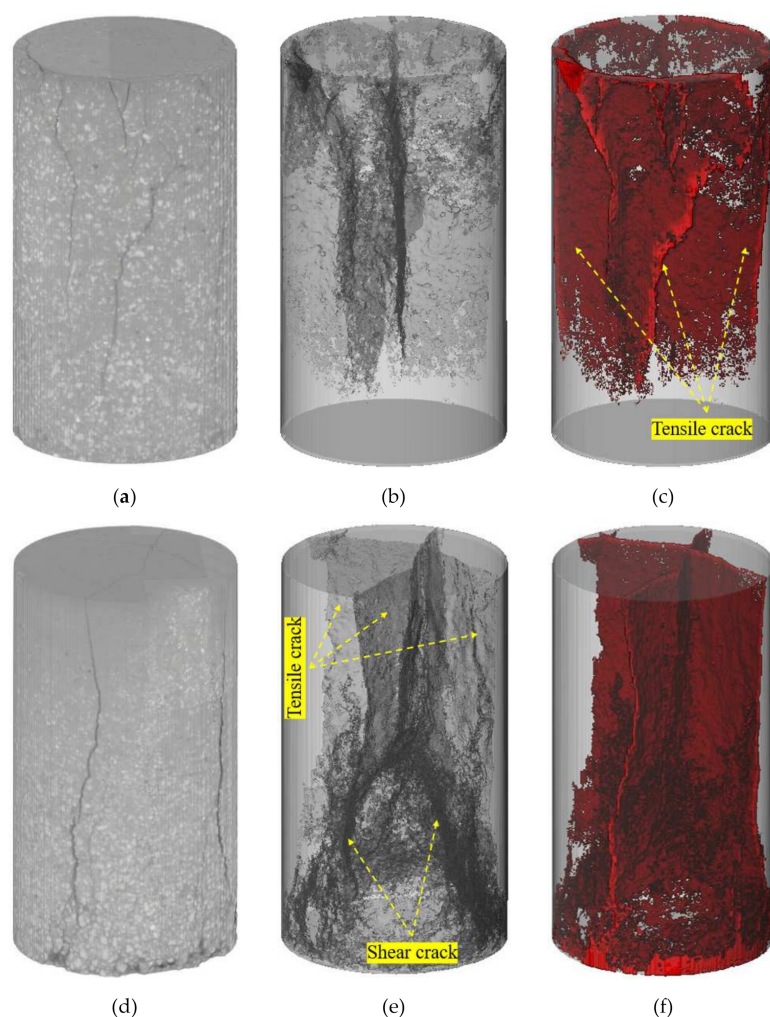


Figure 8. The failure modes of CBC samples. (a–c) Gypsum: 10 wt. %, FA: 50 wt. % and SS: 40 wt. %; (d–f) Gypsum: 10 wt. %, FA: 40 wt. % and SS: 50 wt. %.

It was found that the failure mode of the compressed CBC sample was mainly manifested as a tensile failure from the physical view. The surface and internal tensile cracks through the top and bottom surfaces are shown in Figure 8. Besides, from the perspective view, it could be seen that the internal cracks when the SS content was 40 wt. %, while the internal cracks were not consistent with the observed surface cracks when the SS content was 50 wt. %. The specimen height above 50 mm were mainly tensile cracks, while the height below 50 mm were mostly Y-shaped shear cracks.

As shown in Figure 9, it was also obtained that the cracks were affected by the hindrance of SS particles during the expansion process, which made the expansion direction change. Most of the SS particles were deposited on the bottom due to the increased SS content. The failure modes of CBC samples changed from tensile failure to tensile–shear failure with the increase of SS content from 40 wt. % to 50 wt. %.

3.4. Microstructural Characteristics of Cement-Based Composite Specimens

3.4.1. Effect of Cement on the Microstructure of Cement-Based Composite Specimens

The Image J software was also selected to perform pseudo-color processing on the SEM images to improve the distinguishing qualities of the pictures. Figure 10 shows the SEM images of specimens with different cement contents. According to the SEM image and the morphology of the hydration products, it could be determined that the hydration products in the CBC sample mainly included needle-like ettringite (AFt) and floc-like calcium silicate hydrate (C–S–H) gels.

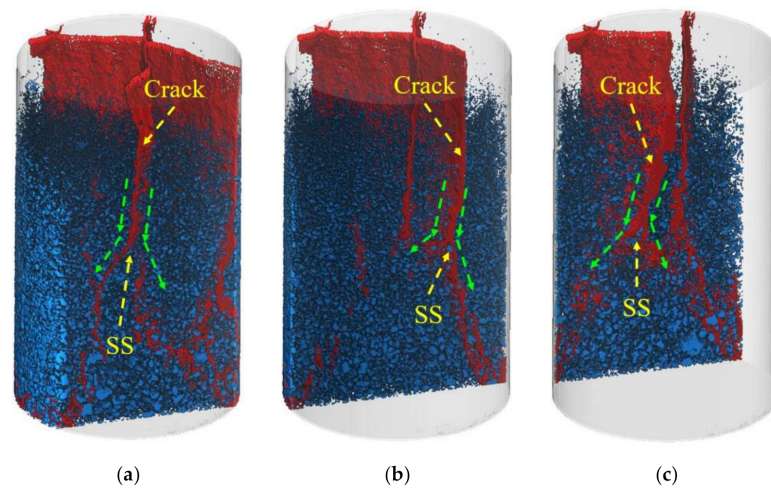


Figure 9. Effect of SS particle cracks propagation direction (Gypsum: 10 wt. %, FA: 40 wt. % and SS: 50 wt. %). (a) $y = 10$ mm. (b) $y = 25$ mm. (c) $y = 40$ mm.

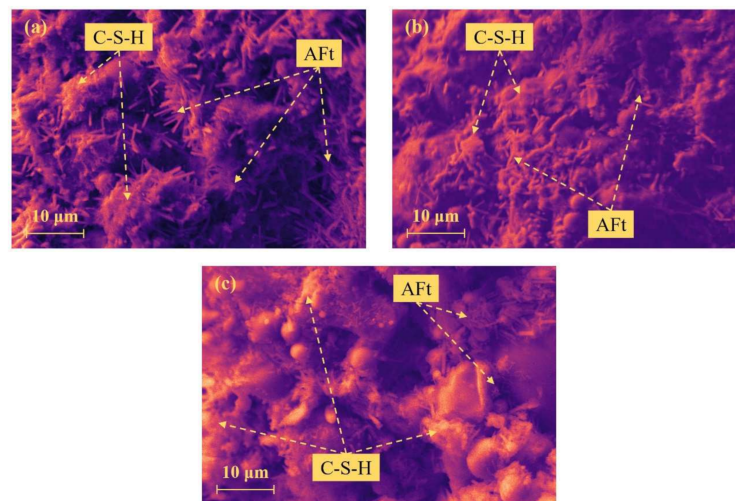


Figure 10. SEM images of CBC samples with different cement content. (a) No cement; (b) 1:12; (c) 1:04.

As shown in Figure 10, it could be found that there were needle-like Aft and floc-like C–S–H gels in the SEM image of NCBC, which indicated that hydration reactions occurred between FA, gypsum and SS. The C–S–H gels generated in the NCBC specimen was less than the others, and the distribution of Aft was sparse. Most Aft hydration products existed independently. Only one end was attached to the surface of solid particles and the other end was not interwoven with further Aft or C–S–H gels. A large number of pores were formed between the solid particles. It was also found from Figure 10b,c that the observable Aft particles decreased and the amount of C–S–H increased when the cement increased. The inside of the CBC became much denser because a large number of hydration products filled the pores between solid particles.

3.4.2. Effects of Gypsum and Fly Ash Content on Microstructure of Cement-Based Composite Specimens

Figure 11 shows the SEM images of CBC samples with different contents of FA and gypsum. It can be seen from Figure 11 that the CBC specimens were much denser when the gypsum and FA were 40 wt. % and 50 wt. %. However, it could be seen from Figure 11b that gypsum particles were irregular in shape, and the particle size of gypsum was more extensive than that of FA. The FA particles with different diameters filled the gypsum particles, while the filling effect was insufficient. There were still large pores among gypsum particles.

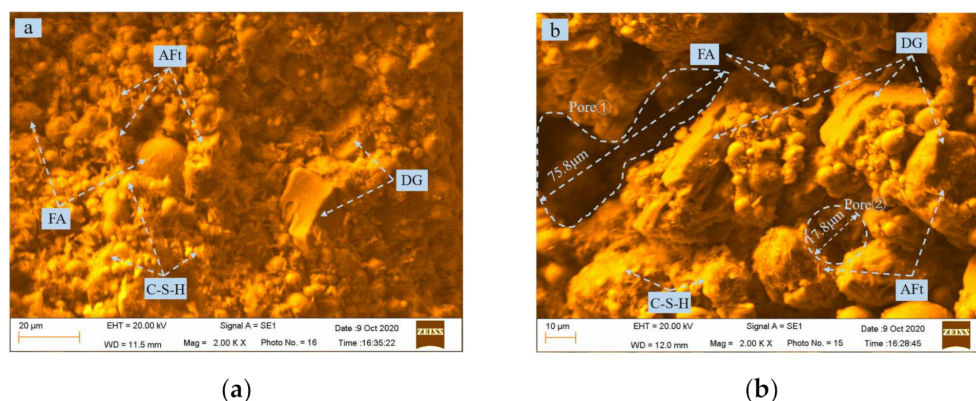


Figure 11. SEM of CBC samples (C/SW ratio was 1:08). (a) Gypsum: 10 wt. %, FA: 50 wt. % and SS: 40 wt. %; (b) Gypsum: 20 wt. %, FA: 40 wt. % and SS: 40 wt. %.

Besides, it could be found that the needle-shaped AFt and C–S–H gels were much more attached to the FA particles' surface and even a small amount of hydration products were attached to the surface of the exposed FA particles. However, there were few hydration products connected to the surface of gypsum particles. For example, the exposed surface of gypsum particles in Figure 11a did not have any hydration products. Hydration products and FA particles only encapsulated the gypsum particles of CBC. Therefore, the UCS decreased when the FA content in the CBC was reduced and the gypsum content increased. This was consistent with the conclusion drawn from the UCS test, and a similar phenomena also appeared in the research results of Li et al. [31].

4. Conclusions

In this study, the effects of cement, FA, gypsum and SS on the UCS and microstructural characteristics of CBC were conducted to investigate the mechanical properties and microstructures. The following conclusions can be drawn as follows:

- (1) The maximum UCS of cement-based composites could reach 6.54 MPa, which could be used as backfilling materials for underground mined-out areas. The UCS increased with the increase of the C/SW ratio, while the elastic modulus increased as the C/SW ratio increased.
- (2) The SS particles have obvious sedimentation during the CBC curing process, and the higher the SS particle content, the more obvious the sedimentation phenomenon happened. The increase in the SS particle content caused the failure modes of CBC to change from tensile failure to tensile–shear failure.
- (3) The increase in cement and fly ash led to a more complete hydration reaction. The internal hydration products of CBC increased and the interior became denser. There were fewer hydration products attached to the surface of gypsum. Additionally, the increase of gypsum content led to the rise of internal pores in CBC.

In the following research, the ratio of gypsum: FA: SS should be further optimized in combination with the conclusions of this research to meet the backfill requirements of underground mined-out areas while reducing the cement content to save costs.

Author Contributions: Conceptualization, S.C.; methodology, J.L.; writing—original draft preparation, J.L.; writing—review and editing and supervision, E.Y. and S.C.; funding acquisition, S.C. All authors have read and agreed to the published version of the manuscript.

Funding: This work was financially supported by the National Natural Science Foundation of China (Grant numbers 51804017), the State Key Laboratory of Silicate Materials for Architectures (Wuhan University of Technology) funds (Grant Number SYSJJ2021-04) and the Fundamental Research Funds for Central Universities (Grant number FRF-TP-20-001A2).

Data Availability Statement: No applicable.

Conflicts of Interest: The authors declare no conflict of interest.

References

1. Ait-Khouia, Y.; Benzaazoua, M.; Demers, I. Environmental desulfurization of mine wastes using various mineral processing techniques: Recent advances and opportunities. *Miner. Eng.* **2021**, *174*, 107225. [[CrossRef](#)]
2. Zhao, Y.; Qiu, J.; Ma, Z. Temperature-dependent rheological, mechanical and hydration properties of cement paste blended with iron tailings. *Powder Technol.* **2021**, *381*, 82–91. [[CrossRef](#)]
3. Huang, Z.; Cao, S.; Yilmaz, E. Investigation on the flexural strength, failure pattern and microstructural characteristics of combined fibers reinforced cemented tailings backfill. *Constr. Build. Mater.* **2021**, *300*, 124005. [[CrossRef](#)]
4. Cao, S.; Xue, G.L.; Yilmaz, E.; Yin, Z.Y.; Yang, F.D. Utilizing concrete pillars as an environmental mining practice in under-ground mines. *J. Clean. Prod.* **2021**, *278*, 123433. [[CrossRef](#)]
5. Li, J.; Yilmaz, E.; Cao, S. Influence of Solid Content, Cement/Tailings Ratio, and Curing Time on Rheology and Strength of Cemented Tailings Backfill. *Minerals* **2020**, *10*, 922. [[CrossRef](#)]
6. Cao, S.; Xue, G.; Song, W.; Teng, Q. Strain rate effect on dynamic mechanical properties and microstructure of cemented tailings composites. *Constr. Build. Mater.* **2020**, *247*, 118537. [[CrossRef](#)]
7. Kang, S.; Ley, M.T.; Behravan, A. Predicting ion diffusion in fly ash cement paste through particle analysis. *Constr. Build. Mater.* **2021**, *272*, 121934. [[CrossRef](#)]
8. Zhao, J.; Su, H.; Zuo, H.; Wang, J.; Xue, Q. The mechanism of preparation calcium ferrite from desulfurization gypsum produced in sintering. *J. Clean. Prod.* **2020**, *267*, 122002. [[CrossRef](#)]
9. Sun, J.W.; Zhang, Z.Q.; Hou, G.H. Utilization of fly ash microsphere powder as a mineral admixture of cement: Effects on early hydration and microstructure at different curing temperatures. *Powder Technol.* **2020**, *375*, 262–270. [[CrossRef](#)]
10. Li, B.Q.; Xie, X.; Lv, J.F.; Zhu, H.; Li, J.; Kang, W.B.; Song, Q. Process and prospect of research on comprehensive utilization of fly ash. *Conserv. Util. Miner. Resour.* **2020**, *5*, 153–160.
11. Li, J.J.; Yilmaz, E.; Cao, S. Influence of industrial solid waste as filling material on mechanical and microstructural characteristics of cementitious backfills. *Constr. Build. Mater.* **2021**, *299*, 124288. [[CrossRef](#)]
12. Duan, S.; Liao, H.; Cheng, F.; Tao, M. Effect of curing condition and carbonization enhancement on mechanical properties of fly ash-desulfurization gypsum—Steel slag blocks. *J. CO₂ Util.* **2020**, *38*, 282–290. [[CrossRef](#)]
13. Solismaa, S.; Torppa, A.; Kuva, J.; Heikkilä, P.; Hyvönen, S.; Juntunen, P.; Benzaazoua, M.; Kauppila, T. Substitution of Cement with Granulated Blast Furnace Slag in Cemented Paste Backfill: Evaluation of Technical and Chemical Properties. *Minerals* **2021**, *11*, 1068. [[CrossRef](#)]
14. Ragipani, R.; Escobar, E.; Prentice, D.; Bustillos, S.; Simonetti, D.; Sant, G.; Wang, B. Selective sulfur removal from semidry flue gas desulfurization coal fly ash for concrete and carbon dioxide capture applications. *Waste Manag.* **2021**, *121*, 117–126. [[CrossRef](#)] [[PubMed](#)]
15. Fu, B.; Liu, G.; Mian, M.; Sun, M.; Wu, D. Characteristics and speciation of heavy metals in fly ash and FGD gypsum from Chinese coal-fired power plants. *Fuel* **2019**, *251*, 593–602. [[CrossRef](#)]
16. Ma, Y.; Nie, Q.; Xiao, R.; Hu, W.; Han, B.; Polaczyk, P.A.; Huang, B. Experimental investigation of utilizing waste flue gas desulfurized gypsum as backfill materials. *Constr. Build. Mater.* **2020**, *245*, 118393. [[CrossRef](#)]
17. Yang, L.; Jing, M.; Lu, L.; Zhu, X.; Zhao, P.; Chen, M.; Li, L.; Liu, J. Effects of modified materials prepared from wastes on the performance of flue gas desulfurization gypsum-based composite wall materials. *Constr. Build. Mater.* **2020**, *257*, 119519. [[CrossRef](#)]
18. Thymotie, A.; Chang, T.-P.; Nguyen, H.-A. Improving properties of high-volume fly ash cement paste blended with β -hemihydrate from flue gas desulfurization gypsum. *Constr. Build. Mater.* **2020**, *261*, 120494. [[CrossRef](#)]
19. Li, Y.; Liu, X.; Li, Z.; Ren, Y.; Wang, Y.; Zhang, W. Preparation, characterization and application of red mud, fly ash and desulfurized gypsum based eco-friendly road base materials. *J. Clean. Prod.* **2021**, *284*, 124777. [[CrossRef](#)]
20. Wang, T.; Wu, K.; Wu, M. Development of green binder systems based on flue gas desulfurization gypsum and fly ash incorporating slag or steel slag powders. *Constr. Build. Mater.* **2020**, *265*, 120275. [[CrossRef](#)]
21. Wansom, S.; Chintasonkro, P.; Srijampan, W. Water resistant blended cements containing flue-gas desulfurization gypsum, Portland cement and fly ash for structural applications. *Cem. Concr. Compos.* **2019**, *103*, 134–148. [[CrossRef](#)]
22. Qi, T.; Feng, Y.Z.G.; Zhang, Y.; Guo, J.; Guo, Y. Effects of Fly Ash Content on Properties of Cement Paste Backfilling. *J. Residuals Sci. Technol.* **2015**, *12*, 133–141. [[CrossRef](#)]
23. Huang, H.; Yuan, Y.J.; Zhang, W.; Hao, R.Q.; Zeng, J. Bond properties between GFRP bars and hybrid fiber-reinforced concrete containing three types of artificial fibers. *Constr. Build. Mater.* **2020**, *250*, 118857. [[CrossRef](#)]
24. Jiang, H.; Yi, H.; Yilmaz, E.; Liu, S.; Qiu, J. Ultrasonic evaluation of strength properties of cemented paste backfill: Effects of mineral admixture and curing temperature. *Ultrasonics* **2020**, *100*, 105983. [[CrossRef](#)]
25. He, Y.; Chen, Q.; Qi, C.; Zhang, Q.; Xiao, C. Lithium slag and fly ash-based binder for cemented fine tailings backfill. *J. Environ. Manag.* **2019**, *248*, 109282. [[CrossRef](#)]
26. Cao, S.; Yilmaz, E.; Yin, Z.; Xue, G.L.; Song, W.D.; Sun, L.J. CT scanning of internal crack mechanism and strength behavior of cement-fiber-tailings matrix composites. *Cem. Concr. Compos.* **2020**, *116*, 103865. [[CrossRef](#)]
27. Li, J.; Zhang, S.Q.; Wang, Q.; Ni, W.; Li, K.Q.; Fu, P.F.; Hu, W.T.; Li, Z.F. Feasibility of using fly ash-slag-based binder for mine backfilling and its associated leaching risks. *J. Hazard. Mater.* **2020**, *400*, 123191. [[CrossRef](#)] [[PubMed](#)]

28. Wei, H.B.; Ba, L.; Gao, Q. Research on the influence of fly ash content on the strength of cemented backfill. *Min. Res. Dev.* **2020**, *40*, 28–32.
29. Li, P.; Cai, M.-F.; Wang, P.-T.; Guo, Q.-F.; Miao, S.-J.; Ren, F.-H. Mechanical properties and energy evolution of jointed rock specimens containing an opening under uniaxial loading. *Int. J. Miner. Met. Mater.* **2021**, *28*, 1875–1886. [[CrossRef](#)]
30. Zhang, S.; Yang, L.; Ren, F.; Qiu, J.; Ding, H. Rheological and mechanical properties of cemented foam backfill: Effect of mineral admixture type and dosage. *Cem. Concr. Compos.* **2020**, *112*, 103689. [[CrossRef](#)]
31. Li, J.J.; Cao, S.; Yilmaz, E.; Liu, Y.P. Compressive fatigue behavior and failure evolution of additive fiber-reinforced cemented tailings composites. *Int. J. Miner. Metall. Mater.* **2021**, *29*, 1–11. [[CrossRef](#)]